Detecting Dissociation Dynamics of Phosphorus Molecular Ions by Atom Probe Tomography

Enrico Di Russo, Ivan Blum, Ivan Rivalta, Jonathan Houard, Gérald da Costa, François Vurpillot, Didier Blavette, Lorenzo Rigutti

Detecting Dissociation Dynamics of Phosphorus Molecular Ions by Atom Probe Tomography

E. Di Russo,* I. Blum, I. Rivalta, J. Houard, G. Da Costa, F. Vurpillot, D. Blavette, and L. Rigutti

ABSTRACT: Dissociation processes involving phosphorus cations were investigated during laser-assisted atom probe tomography of crystalline indium phosphide (InP). This technique not only allows the formation of medium-sized phosphorus cations by means of femtosecond laser pulses under ultrahigh vacuum and high electric field conditions but also allows one to study the time-resolved dissociation dynamics. Data reveal the formation of cations up to P232+ and their subsequent dissociation into two smaller Pk+ cations (k > 2). The use of a time- and position-sensitive detector combined with numerical calculations provided information related to the molecule orientation, decay time, and kinetic energy release during dissociation phenomena. Results suggest that the dissoci-ation processes are most likely due to the emission of Pk2+ cations in excited states and their subsequent decay in low field regions during their flight toward the detector. This study provides operative guidelines to obtain information on dissociation processes using a tomographic atom probe as a reaction microscope and indicates the current capabilities and limitations of such an approach.

1. INTRODUCTION

Laser-assisted atom probe tomography (La-APT) is an analytical microscopy technique that allows one to investigate at the atomic scale both the three-dimensional atomic distribution and the composition of a needle-shaped specimen presenting a curvature radius of about 50−100 nm. Such a technique has been adopted in the last few years for the study of a wide range of semiconductor-based materials and devices (i.e., light-emitting diodes, quantum cascade lasers, nanowires, solar cells, multiquantum confined systems for optoelectronic applications).[1−6] Atom probe tomography relies on the field evaporation of surface atoms of the analyzed sample. The high electric field needed (a few tens of $V{\cdot}nm^{-1}$) requires the specimen to be prepared in the form of a sharply pointed tip that is submitted to a high positive voltage. Surface atoms are field-evaporated in the form of positive ions (cations) in a well-controlled way using very short intense laser pulses (<1 ps, 100 000 pulses/sec) superimposed to the steady-state field generated. Field-evaporated ions repelled by the positive voltage present at the tip surface are accelerated toward a position- and time-sensitive detection system (PTSD). This latter allows determining both the position of ion impacts and the chemical nature of each single cation by time-of-flight (TOF) mass spectrometry.

The formation of molecular ions is very frequent in APT analyses of dielectric materials. Such molecular ions lead to biased composition data if not fully understood and considered. Several studies have revealed that the abundance of molecular ions can be controlled by varying the electric field at the tip surface.[7−15] Recently, the adoption of advanced data-processing methods has given access to the dynamics of dissociation, such as the molecule orientation or the energy dissipated during the process.[16,17]

In this article, we report on an in-depth study of dissociation of large-sized phosphorus P_k^{j+} $(k \geq 1; j \geq 1)$ cations generated during the field evaporation of InP semiconductors. In past studies, the stability of phosphorus clusters was investigated through time-of-flight (TOF) mass spectrometry: experiments based on collision-induced dissociation processes of mass-selected phosphorus cations or in laser ablation have already been attempted.[18,19] However, such approaches do not provide direct access to dissociation dynamics of reactions due to the lack of temporal resolution at their time scale: consequently, result interpretation could be difficult and ambiguous. These issues can be circumvented by an approach based on atom probe tomography. This technique presents a unique opportunity to directly observe the dissociation processes, providing also access to quantitative information regarding the

dynamics of dissociation processes at the nanosecond time scale.

2. EXPERIMENTAL AND THEORETICAL METHODS

2.1. Laser-Assisted Atom Probe Tomography. To perform La-APT, InP tips were prepared along the [001] direction by a standard scanning electron microscopy/focused ion beam (SEM/FIB) lift-out procedure followed by annular milling with 30 kV Ga ions and a cleanup procedure at 2 kV.[20,21] Because the occurrence frequency of dissociation processes detected during La-APT is very low, a large volume of InP must be analyzed to maximize the number of recorded dissociation events. To do so, a single 3 μm long needle-shaped specimen with a tip initial diameter of about 80 nm and a cone angle of 3° was entirely analyzed. Atom probe analysis was performed using a laser-assisted wide-angle tomographic atom probe (LaWaTAP) operated with femtosecond laser pulses (350 fs) at a wavelength of λ = 515 nm (green). The pulse repetition frequency was 100 kHz. The laser pulse energy E_{las} was 3 nJ, corresponding to a peak energy density during the pulse of 1.5×10^{-4} J·cm^2. The detection system used was a custom-designed multichannel plate/advanced delay line detector (MCP/aDLD) with an MCP detection efficiency $\eta_{MCP} \approx 0.6$, with diameter D = 7.6 cm. Such a system is improved for the multihit detection.[22,23] The La-APT analysis was performed at a constant detection rate ($\varphi \approx 0.0025$ event/pulse), varying the applied bias V_{DC} to keep φ constant during the tip evaporation. Under these conditions, the entire InP tip was evaporated in about 10 days. The acquired data set consists of 7×10^7 ions. The specimen base temperature (T_{base}) was maintained at 50 K. Field evaporation of surface atoms is promoted by laser pulses that increase temporarily the temperature reached at the tip surface.[24,25] This temperature is thus pulsed at the same frequency as the laser, which is 100 kHz.

2.2. Electric Field Calculations. Following the approach described in previous works,[15,16,26,27] numerical calculations were performed using an electrostatic model of the atom probe used (LaWaTAP). The simulated configuration consists of two confocal paraboloids. The first one represents the analyzed InP field emitter tip, with curvature radius at the apex R = 100 nm. This is held at a potential of V_{DC} = 11 kV. The second paraboloid mimics the detector and is held at the ground potential. Due to the axial symmetry of such a configuration, a cylindrical coordinate system (r,z) was adopted. The z-axis is directed along the symmetry axis of the field emitter; the r-axis is perpendicular to the z-axis (see Figure 2). The electric potential distribution between the field emitter and the screen is provided by the simple equation

$$V(r, z) = a \ln\left(\frac{r+z}{2L}\right) \tag{1}$$

where $a = \frac{V_{DC}}{\ln\left(\frac{z_0}{L}\right)}$, L = 10 cm is the distance between the tip and detector, and z_0 = 50 nm is the focal length associated with the parabolic shape of the field emitter. This last is described by the following equation

$$r^2 = 4z_0(z_0 - z) \tag{2}$$

It should be remembered that the relation between the focal length z_0 and the curvature radius R is as follows: $2z_0 = R$. For this reason, the position of the field emitter apex is (0, R/2).

Finally, the electric field $\vec{E}$ was calculated using the following relation: $\vec{E} = -\vec{\nabla} V$. The components ($E_r$,$E_z$) of the electric field are given by

$$E_r(r, z) = -\frac{ar}{r^2 + z^2 + z^2\sqrt{r^2 + z^2}} \tag{3}$$

$$E_z(r, z) = -\frac{a}{\sqrt{r^2 + z^2}} \tag{4}$$

The distribution of the electric field intensity $E(r,z)$ was calculated in the vicinity of the tip using eqs 3 and 4. Results are represented in Figure 1a. The distribution reveals that high

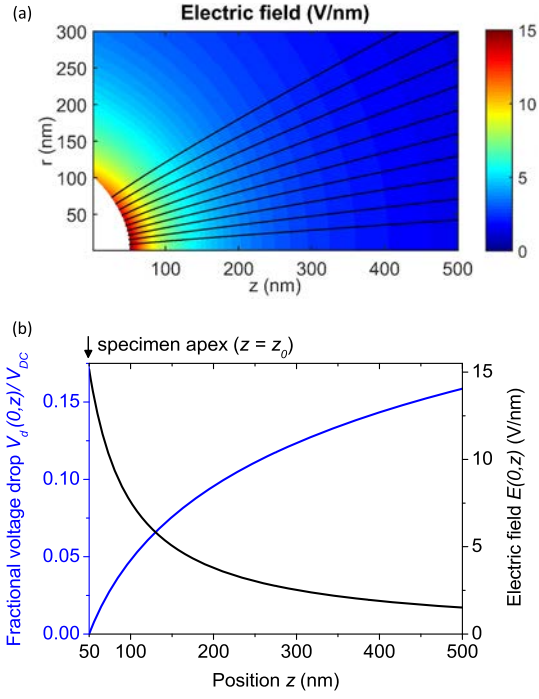

Figure 1. (a) Distribution of the electric field $E(r,z)$ and ion trajectories around a parabolic tip. The simulation parameters are as follows: curvature radius of 100 nm; V_{DC} = 11 kV; tip−detector distance L = 10 cm. The z-axis corresponds to the tip symmetry axis. The specimen is represented in white. (b) Details of the relationships between both the fractional voltage drop $V_d(0,z)/V_{DC}$ and the magnitude of the electric field $E(0,z)$ as a function of the distance z ranging between z_0 = 50 nm and z = 500 nm.

field conditions correspond only to a region limited to about 100 nm from the specimen surface. The field intensity profile extracted along the specimen-detector axis $E(0,z)$ is plotted as a function of the distance z in Figure 1b. According to the above parameters, the field intensity corresponding to the specimen apex at ($z = R/2$) is equal to 15.2 V·nm^{-1} at. This field quickly decreases with the increase in distance z. At z = 150 nm, that is, 100 nm away from the specimen apex ($z = z_0$), the field intensity is drastically reduced to 5 V·nm^{-1}. It should be noted that the real atomic structure of the tip surface (e.g., terraces, terrace edges, atom groups, etc.) is ignored in this model. The presence of such surface structures and their evaporation during analyses induces important local variations of the electric field distribution on the tip that are not considered here. Finally, the fractional voltage drop $\frac{V_d(r,z)}{V_{DC}} = 1 - \frac{V(r,z)}{V_{DC}}$ calculated along the specimen-detector

axis ($r = 0$) is plotted in Figure 1b using eq 1. It should be noted that the fractional voltage drop along the selected ion trajectory presents a linear dependence with respect to the logarithm of z (see also Figure 7c).

Note that the fractional voltage drop $V_d(r,z)/V_{DC}$ only depends on the geometry of the field emitter and the position of the detector. The same consideration can be extended also to the shape of both electric field lines and ion trajectories. The field lines are described by paraboloids

$$(z + b)^2 = z^2 + x^2 \tag{5}$$

where b is a constant related to each field line. The cation trajectories were computed using the Newton equation that was solved by numerical integration adopting the half-step velocity Verlet algorithm

$$m\vec{a}(t) = q\vec{E} \tag{6}$$

where $\vec{a}$ is the cation acceleration vector, $\vec{E}$ is the electric field vector, and t is the time ($t = 0$ is the moment when an ion leaves the sample surface). The algorithm implementation scheme is as follows

(i) calculate:

$$r(t + dt) = r(t) + v(t)dt + \frac{1}{2}a(t)dt^2 \tag{7}$$

(ii) derive:

$$a(t + dt) \text{ in the position } r(t + dt) \text{ using} \tag{8}$$

eq 6

(iii) calculate:

$$v(t + dt) = v(t) + \frac{1}{2}a(t + dt)dt \tag{9}$$

where $\vec{r}$ and $\vec{v}$ are the cation position and velocity vectors, respectively; dt was set equal to 10^{-14} s. The ion trajectories calculated for LaWaTAP under the above-mentioned conditions are depicted in Figure 1a. More details about the cation trajectories in a field ion microscope are reported in ref 26.

2.3. Dissociation Dynamic. A classical model of molecular ion dissociation dynamic in atom probe was recently proposed in ref 11. The approach adopted is essentially the same used to study the fragmentation of molecular ions by an intense picosecond laser introduced in ref 28. When a parent molecular ion with a mass-to-charge ratio m_p is emitted from the tip, this is accelerated toward the detector thanks to the presence of the electric field. During the flight toward the detector, the parent molecular ion can be dissociated into two charged fragments. As illustrated in Figure 2, this reaction can be schematized as follows: $m_p \rightarrow m_1 + m_2$. However, because the energies of daughter ions are affected, their measured mass-to-charge ratios m'_1 and m'_2 are different compared to the mass-to-charge ratio m_1 and m_2 measured for identical ions directly emitted from the tip. Such a difference increases as the distance of the dissociation point from the tip surface is greater. The measured mass-to-charge-state ratio m'_i of a generic daughter ion ($i = 1, 2$) is expressed by the following equation

$$m_i' = m_i\left[1 - \frac{V_d}{V_{DC}}\left(1 - \frac{m_i}{m_p}\right)\right]^{-1} \tag{10}$$

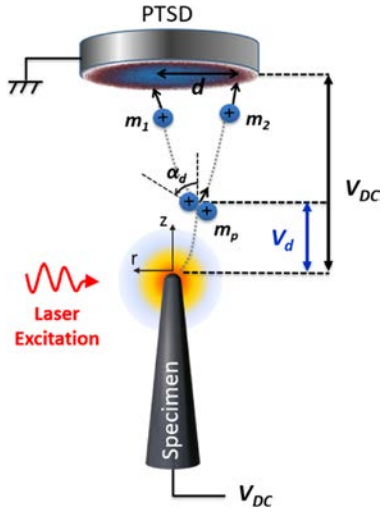

Figure 2. Schematic representation of a dissociation process: a mother cation with a mass-to-charge ratio m_p dissociates into two fragments with mass-to-charge ratios m_1 and m_2. V_{DC} is the DC voltage applied to the tip, and V_d is the potential drop after which the dissociation occurs.

where V_{DC} is the DC voltage applied to the tip and V_d is the potential drop after which the dissociation occurs, as illustrated in Figure 2. It should be noted that the fractional voltage drop V_d/V_{DC} is the only parameter fixing the detected mass-to-charge ratio m'_i of a daughter ion. Only if $V_d \approx 0$ (dissociation very close to the tip surface), the detected mass-to-charge ratio m'_i is close to m_i. If dissociation occurs after a voltage drop $V_d \gg 0$, a mass-to-charge ratio $m'_i < m_i$ is measured for the most massive daughter ion, while $m'_i > m_i$ is observed for the second ion. Clearly, V_d/V_{DC} can be easily calculated for each single daughter ion measuring its mass-to-charge ratio m'_i.

As detailed in ref 16, molecules that dissociate parallel to the electric field (dissociation angle $\alpha_d = 0$ or 180°) will produce impacts very close to each other on the detector (impact distance $d \approx 0$ mm). In this situation, daughter ions propagate along the same trajectory. However, the Coulomb repulsion acting between daughter ions immediately after the dissociation of parent cations leads to the acceleration of the first daughter ion toward the detector, while the second one is delayed as subjected to an acceleration toward the tip. If we consider a molecular ion composed of two atoms with the same mass, this will lead to a slight difference in their time of flight and of the calculated mass-to-charge ratio of daughter ions ($m_1 - m_2 > 0$ Da). In contrast, if the dissociation direction is perpendicular to the electric field ($\alpha_d = 90°$), daughter ions of the same mass reach the detector at the same time, leading to the same mass-to-charge ratio ($m_1 - m_2 = 0$ Da). However, in this case, the Coulomb repulsion produces a lateral acceleration between daughter ions, increasing their impact distance on the detector ($d > 0$ mm). This is true whatever the mass of ions. In addition, the shorter the lifetime of the parent cation, the larger the impact distance d. This is partly due to the higher divergence of the electric field lines close to the tip surface, which magnifies the dispersion of the ions originating from dissociation events occurring close to the tip.

3. RESULTS AND DISCUSSION

3.1. Mass Spectrum. In Figure 3 is reported the mass spectrum of the analyzed InP specimen. Two peaks associated

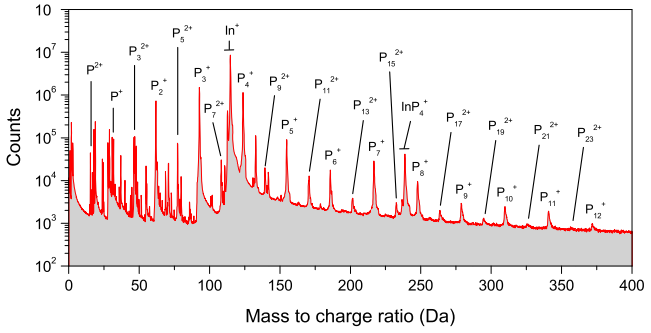

Figure 3. InP mass spectrum. Parameter used: detection rate $\varphi \approx 0.0025$ event/pulse; laser peak energy density 1.5×10^{-4} J·cm^2 (green); $T_{base} = 50$ K. The number of ions detected is about 7×10^7.

with In^+ isotopes are observed at 113 and 115 Da (natural abundances: $^{113}In = 4.3\%$; $^{115}In = 95.7\%$), but no peak at 56.5 and 57.5 Da reveals the presence of In^{2+} ions in the data set. It should be noted that the simultaneous presence of two charge states of a given species (i.e., In^+ and In^{2+}) in the mass spectrum would allow determining the charge-state ratio (i.e., In^{2+}/In^+). Such a quantity can then be directly linked to the average (in time and space) electric field intensity at the tip surface. To do so, the so-called effective field F_{eff} is calculated through Kingham's postionization model.[4,8,12,29−31] Because no In^{2+} ions are formed, the Kingham theory predicts that F_{eff} is below 20 V·nm^{-1}. This estimate is compatible with the electric field calculated at the center of the tip using eq 4, which is $E = 15.2$ V·nm^{-1}.

In the cases of III−V semiconductors (e.g., GaN, GaAs, GaSb), measurements performed at low F_{eff} promote the evaporation of V-group molecular ions rather than singly ionized atoms. A detailed study was recently reported in the case of GaAs, where the formation of larger As_k^{j+} ($k \geq 1$; $j \geq 1$) cations was observed when decreasing the applied electric field.[8] Similar conclusions were reported for Sb_k^{j+} cations in GaSb.[9] The present study of InP reveals the presence of numerous peaks related to phosphorus ($m = 31$ Da) molecular ions in the mass spectrum (Figure 3). Peaks observed at $(31 \times k/j)$ Da are related to P_k^{j+} cations. It should be mentioned that in the InP cubic crystal structure, phosphorus atoms have only indium atoms as first neighbors and no P−P or In−In bonds exist. However, phosphorus may slightly migrate at the tip surface during the field evaporation of the specimen, leading to the formation of phosphorus clusters that field-evaporate in the form of molecular ions.[32] Short-range surface migration can indeed occur for group-V atoms due to the combination of laser heating effects and local field gradients.[33] This hypothesis is supported by studies showing that group-V atoms have a low activation energy for diffusion and thus high surface diffusion coefficients.[34] However, as recently demonstrated in the case of GaAs, the detection of larger As_k^{j+} cations is insensitive to the laser pulse energy under La-APT standard analysis conditions.[8] This means that both the size and the relative abundances of molecular ions do not increase significantly with the surface temperature but are mainly controlled by the field intensity.

Because phosphorus has only one stable isotope, P_k^{j+} and P_{2k}^{2j+} cations have the same time-of-flight and form perfectly overlapped peaks in the mass spectrum. Such an issue is due to technological limitations of the detection system currently employed, which does not allow one to discriminate ions arriving with the same time-of-flight but different kinetic energies. In fact, the signals propagating through the DLD are insensitive to the nature, mass, and energy of the cations that impact the MCP. In the future, the use of detectors based on superconductor materials could allow discriminating cations by measuring their kinetic energy as well.[35] However, phosphorus is an odd-electron atom, so only P_k^+ with k odd and P_{2k}^{2+} cations present no dangling bonds and a more stable configuration. As a consequence, the peak intensities associated with odd-sized cations are generally higher than the ones associated with even-sized cations.[19,36] In Figure 3, such an alternation of the peak intensities is not observed. This could be due to a peak associated with P_{2k}^{2+} ions superimposed on the one associated with P_k^+ ions.

Lastly, a second regular series of peaks was associated with P_{2k+1}^{2+} ions ($k \geq 1$). The peaks at 237 and 239 Da are then associated with the presence of InP_4^+ molecular ions. Parasitic species (such as hydrogen-, carbon-, nitrogen-, and oxygen-related peaks) and hydrides were also detected, most likely supplied by the environment during the tip preparation procedure and during La-APT analysis.

3.2. Multiple Detection Events. In atom probe tomography, the analysis of multiple detection events allows drawing important conclusions about biases induced by specific detector limitations,[8,15,37] dissociation phenomena that involved molecular ions,[8,11−13,16] and correlated evaporation processes.[8,38] A multiple-ion event consists of the detection of two or more ions following the same laser pulse. In the MCP/aDLD detector used here, the spatial resolving power is 1.5 mm (MCP active surface diameter ≈ 7.7 cm) and the time resolving power is 1.5 ns.[22,23] Signals related to multiple impacts of ions with close times of flight (<1.5 ns) and impact distance d < 1.5 mm are convoluted in a single signal, making the detection of multihits impossible.[8,16,23] This phenomenon is commonly known as the "pile-up effect".

The histogram representing the fraction of multiple events is reported in Figure 4a. The fraction of multiple events of order n = 1, 2, ... corresponds to the fraction of detection events associated with the n ions recorded following the same laser pulse. In the data set that is analyzed here, the number of ions associated with multihits is 2.4×10^6. Only 1.5% of the detection events are associated with double hits, while only 0.13% is associated with the simultaneous detection of three ions. The percentage of events involving the number of hits equal to or higher than 4 ions is 0.02%. It should be noted that the probability of detecting a single ion is limited by the multichannel plate efficiency ($\eta_{MCP} \approx 0.6$). As a consequence, the probability of detecting double impacts is reduced to $\eta_{MCP}^2 \approx 0.36$ and to $\eta_{MCP}^3 \approx 0.22$ for triple impacts. This means that at least about two-thirds of the effective number of ions arriving almost simultaneously on the detector cannot be recognized as multihits but are either detected as single events or completely undetected. The distribution of the detection distances d between ion hits within multiple events is reported in Figure 4b. This distribution is bimodal with two contributions. In fact, it is possible to observe a peak at small distances with a maximum at 1.4 mm, corresponding to spatially correlated near-simultaneous events, and a broader distribution shifted toward larger detection distances that is associated with uncorrelated events. It should be noted that these distributions are the convolution of various distributions associated with correlated evaporation phenomena, molecule dissociation processes, and uncorrelated multiple evaporation

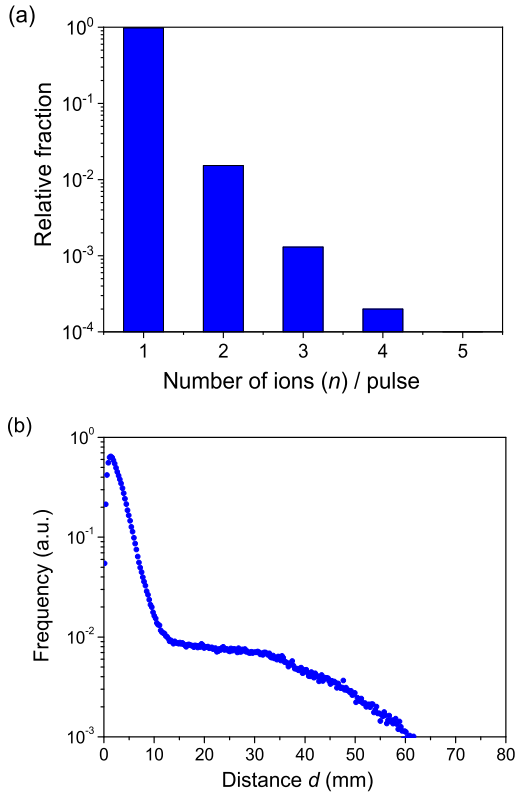

Figure 4. (a) Histogram of the fraction of multiple detection events and (b) distribution of distances between impacts associated with multiple events for the InP mass spectrum reported in Figure 1.

events.[8,12,16,38,39] The presence of a fast drop for d <1.4 mm is related to the above-mentioned resolution limitations of the detector both in space and in time and has been recently highlighted in other experimental and simulated data sets.[8,15,37] It should be noted that the influence of pile-up effects on the measured composition strongly depends on the material evaporation behaviors and not only on the performance of a specific detection system.[8,23] The selective loss effects must be therefore evaluated in each specific case.

3.3. Correlation Histogram and Dissociation Processes. The correlation histogram associated with the analyzed data set is reported in Figure 5. In this histogram, all of the $\{m_1,m_2\}$ ion pairs detected in multiple-ion events are represented (the subscripts 1 and 2 represent two generic cations). In the case of multiple events in which three ions are detected, all possible permutations of ion pairs that are involved were taken into account, for example, a triple event in which m_1, m_2, and m_3 ions are detected is spitted into the following ion pairs: $\{m_1,m_2\}$, $\{m_2,m_3\}$, and $\{m_1,m_3\}$. Multiple events with $n > 3$ were not considered because their contribution is negligible (see Figure 4a). In a correlation histogram, the ion-pair detection order is not taken into account; therefore, a pair $\{m_1,m_2\}$ is equivalent to the pair $\{m_2,m_1\}$. Here, a symmetry axis was thus added on the diagonal of the diagram, making each pair represented twice.

Correlation histograms provide important information regarding both correlated evaporation phenomena and dissociation reactions that can be obtained. First of all, ion pairs leaving the tip in coincidence with laser pulses lead to the detection of ions with the expected mass-to-charge ratios. Such events can be identified, for example, as yellow/red spots in Figure 5. Moreover, several tracks can be distinguished in correlation histograms. Horizontal and vertical tracks are associated with the field evaporation of an m_1 ion in agreement with a laser pulse, followed by the evaporation of an m_2 ion after the time interval Δt. In this case, the detected mass-to-charge ratio associated with the m_2 ion is larger compared to the expected one. Lines or curves with a positive slope are associated with the simultaneous delayed evaporation of both m_1 and m_2 ions at time Δt after the tip heating provided by a laser pulse. In this latter case, both ions are detected with mass-to-charge ratios larger than the expected ones. Such delayed evaporations are explained in terms of the slow cooling along the specimen after the laser pulse and can be in part reduced by decreasing the laser energy $E_{las.}$.[8,40] These events lead to long tails in the mass spectrum that cannot be considered in single ion counting because of large multiple overlaps. This reduces the accuracy of composition measurements.

In correlation histograms, the more interesting curves exhibit a negative slope. These are associated with dissociation processes of mother molecular ions fragmented into two daughter ions.[8,11−13,16]

Last, it should be mentioned that the presence of dissociation tracks in correlation histograms depends on the design of the tomographic atom probe that is used. Briefly, after a dissociation process, the daughter heavier ion has an excess of kinetic energy (i.e., $m'_i < m_i$), while the lighter one presents a kinetic energy deficit (i.e., $m'_i > m_i$). In the worst case, when dissociation takes place with a significantly large delay, the final velocity of both fragments is similar and close to the velocity of the parent ion. Assuming a dissociation of a phosphorus cluster, such as $P_n^{2+} \rightarrow P_k^+ + P_m^+$ with $n = k + m$, the kinetic energy of both fragments will be $Ec_k = \frac{k}{k+m}Ec$ and $Ec_m = \frac{m}{k+m}Ec$, with Ec being the kinetic energy of the mother molecule accelerated by the tip held at voltage V_{DC}. The simplest case such as $P_5^{2+} \rightarrow P_3^+ + P_2^+$ or $P_6^{2+} \rightarrow P_4^+ + P_2^+$ gives deficit/excess in energies larger than 20%. When dissociation takes place close to the tip, differences in energies account generally for a few percent. In this case,

$$Ec_k = \left[1 + \delta\left(\frac{2k}{k+m} - 1\right)\right]\frac{Ec}{2} \tag{11}$$

and

$$Ec_m = \left[1 + \delta\left(\frac{2m}{k+m} - 1\right)\right]\frac{Ec}{2} \tag{12}$$

δ is here defined by $1 - V_d/V_{DC}$, the relative deficit in voltage where the dissociation takes place.

In a tomographic atom probe equipped with a reflectron lens, the difference in kinetic energy and kinetic energy spread can be in part compensated, resulting in only partial molecular dissociation tracks. In this way, the information regarding dissociation processes is partially suppressed.[13,15,41] This compensation is described in different textbooks, and it can be proven that the first-order deficit $\pm\delta$ is transformed into the positive second-order term δ^2. We may note that ions with too much excess in kinetic energy (or more rigorously in equivalent acceleration voltage of the charge particle) may be filtered by the device. The reflectron is composed of an electrostatic mirror held at a voltage $c_{REF}\cdot V_{DC}$. This voltage is applied to the back-end metallic anode of the mirror. The coefficient c_{REF} is adjusted to optimize the performance of the

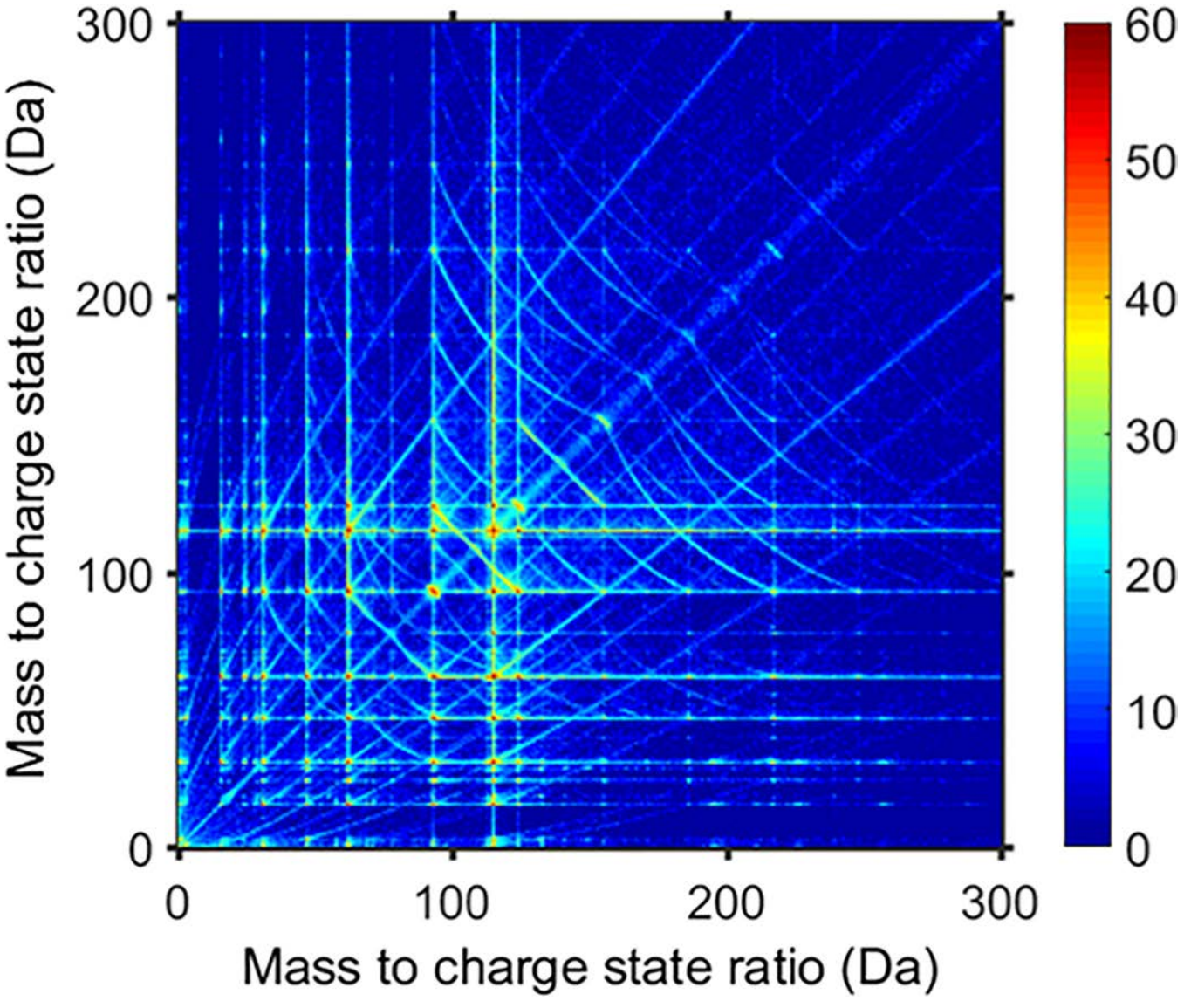

Figure 5. Correlation histograms of InP associated with the mass spectrum of InP reported in Figure 3. The color scale represents the number of detected pairs.

mass spectrometer and is generally in the range 1.01−1.05.[42] It means that ions accelerated by voltages higher by 5% than V_{DC} simply hit the back-end electrode and are lost.

As a result, as described in Figure 6, four different dissociation cases may be considered theoretically in a reflectron-based atom probe. When the dissociation is fast and takes place close to the tip, the energy deficit/excess of both daughter ions is small and compensated by the device (for excess in energy <5%) (Figure 6a). As described in ref 15, the dissociation track is then compressed close to the pair $\{m_1;m_2\}$ (Figure 6e, track i). When the excess in energy is higher than ∼5% (Figure 6b), the ion with excess energy hits the back-electrode and the track is lost (Figure 6e, track ii). When the dissociation takes place in the reflectron, with a delay large enough to avoid filtering the ion in energy excess (Figure 6c), the dissociation is then very delayed (>100 ns) and partial compensation of kinetic energy occurs. This case is normally recognized as a pair of hits with an equivalent mass-to charge ratio equal to $(m_1 + m_2)/(n_1 + n_2)$ in a standard linear atom probe. The same effect is observed in a reflectron-based tomographic atom probe when dissociation occurs after passing through the compensation device (Figure 6d). In the reflectron, depending on the depth at which the dissociation occurs, the compensation amplitude is different, and the final time of flight on the detector of the ion with excess energy is increased, whereas the time of flight of the ion with energy deficit is decreased. A new dissociation track will then be produced (Figure 6e, track iii) compared to the standard atom probe, which may explain why some large tracks may be visible in reflectron-based machines. In all cases, the presence of the reflectron much complicates the interpretation of dissociation tracks in correlation histograms.

The same conclusion can be extended to the case of the FlexTAP instrument (Figure 6f). This tomographic atom probe is equipped with electrostatic lenses, which modulate the ion trajectories and also act as an energy dispersion filter. Converse to the reflectron, electrostatic lenses are low-energy ion filters.[43,44] The electrostatic lens used to deflect and compress ion trajectories are equivalent to an electrostatic voltage barrier. The cutoff voltage is generally 95% of the tip

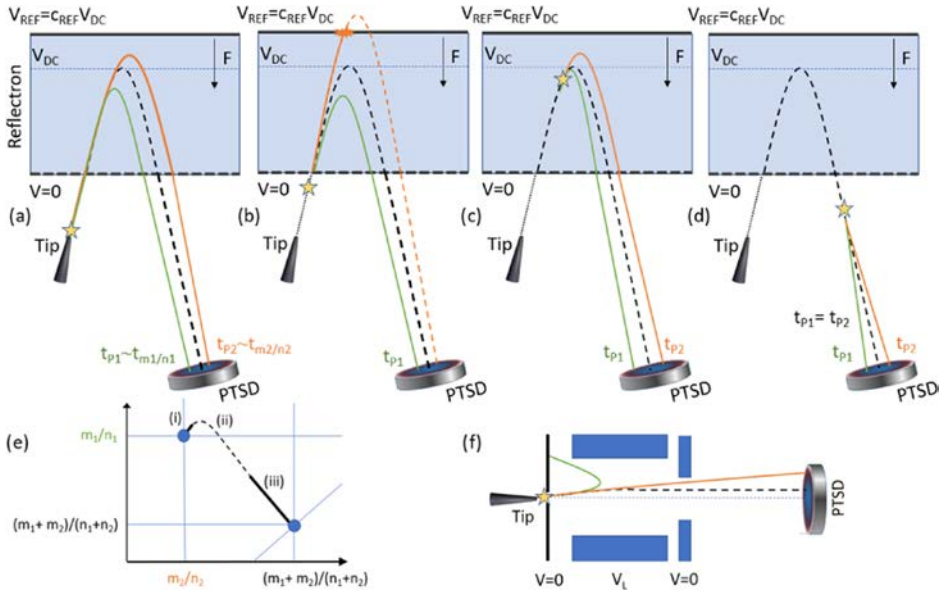

Figure 6. Schematic representation of different dissociation cases in a reflectron-based atom probe: (a) dissociation close to the tip; (b) dissociation excess in energy higher than ∼5%; (c) dissociation in the reflectron; and (d) dissociation after passing through the reflectron. (e) Schematic representation of the correlation histogram in a reflectron-based tomographic atom probe. (f) Schematic representation of a dissociation process in a FlexTAP for the daughter ion with energy deficit higher than 3−4%.

voltage (Figure 6f). In this case, only daughter ions with energy deficit lower than 3−4% will be visible as dissociation tracks. In this case, dissociation tracks will be deformed by the deceleration/acceleration zones existing on the path of ions.

The use of a straight flight path tomographic atom probe such as a CAMECA LaWaTAP or LEAP Si series instrument is therefore recommended to study dissociation processes.

3.4. Heterolytic Phosphorus Cation Dissociation Processes. In the correlation histogram depicted in Figure 5, a large number of negative slope tracks is associated with the dissociation processes of phosphorus cations. Both mother and daughter ions associated with each of these processes were identified by fitting experimental data with eq 10. The data reveal that the dissociation of P_k^{2+} cations with $4 \leq k \leq 15$ occurs. The smallest unstable cation is P_4^{2+}, which dissociates in P_3^+ and P^+. This clearly indicates that the peak at 62 Da is associated with a mix of P_2^+ and P_4^{2+} cations. Experimental data also show that P_5^{2+} cations dissociate as follows: $P_5^{2+} \rightarrow P_3^+ + P_2^+$. It should be noted that also the dissociation process $P_5^{2+} \rightarrow P_4^+ + P^+$ is possible because both mass and electric charge are conserved. Nevertheless, this reaction is not observed in the correlation histogram. As a general rule, it will be shown that the dissociation processes of phosphorus cations leading to the formation of monoatomic P^+ ions are not favored. This can be ascribed to the structure of phosphorus cations assembled on the tip surface. In fact, the formation of P_2, P_3, and in particular P_4 subunits is energetically more favorable than larger phosphorus cations.[45−47] This is confirmed by atom probe data, where P_3^+ and P_4^+ ions appear as the most abundant species in the mass spectrum (Figure 3). Similar conclusions were observed in collision-induced experiments performed by Huang et al. in ref 18. Continuing the analysis of the correlation histogram, it was found that P_6^{2+} cations dissociate through a unique dissociation pathway: $P_6^{2+} \rightarrow P_4^+ + P_2^+$.

The dissociation of P_7^{2+} cations is the most interesting case. In fact, the dissociation track corresponding to the only allowed process $P_7^{2+} \rightarrow P_4^+ + P_3^+$ appears particularly intense in the correlation histogram in Figure 5. Such a process is highlighted in Figure 7a. Density functional calculations performed clearly evidence that P_7 clusters are in fact most likely formed by a P_4 roof structure bond with a P_3 unit.[48] In addition, the peak associated with P_7^+ ions in the mass spectrum dominates compared to neighbor peaks, which are associated with P_6^+ and P_8^+ ions (see Figure 3). The ratios associated with the relative abundances are, respectively, $P_7^+/P_6^+ = 1.9$ and $P_7^+/P_8^+ = 2.8$. A similar trend in the relative peak intensities is reported also for cations generated in mass spectra collected following laser ablation processes.[49,50]

To obtain more information regarding the dynamic of the dissociation reaction $P_7^{2+} \rightarrow P_4^+ + P_3^+$, all of the ion pairs $\{P_4^+;P_3^+\}^{\text{diss.}}$ recognized in the entire dissociation track were selected. However, only the pairs of ions that exhibit a measured m close to the expected value m'_i within 0.1 Da (eq 10 for $i = P_4^+, P_3^+$) were considered. In the correlation histogram, the dissociation track overlaps the signal associated with the correlated evaporation involving $\{P_4^+;P_3^+\}^{\text{corr.}}$ ion pairs. Thus, only the ion pairs with a fractional potential drop $(V_d/V_{DC}) > 0.015$ were selected. Of course, a significant contribution of P_7^{2+} cation dissociation close to the tip surface is possible (i.e., $V_d/V_{DC} \approx 0$), but these cannot be unambiguously identified as such when adopting such an approach.

In Figure 7b, the histogram of the number of ion pairs as a function of the distance between the impacts of two daughter ions (d) and the fraction of the potential drop (V_d/V_{DC}) is depicted. The data show that both the interimpact distances and the number of dissociation events decrease with V_d/V_{DC}. This last piece of information is highlighted in Figure 7c, where the distribution of the dissociation events as a function of the fractional potential drop (V_d/V_{DC}) is represented. Data show a decreasing distribution, without a predominant contribution for dissociations occurring close to the tip. Such behaviors strongly suggest that the principal dissociation process of P_7^{2+}

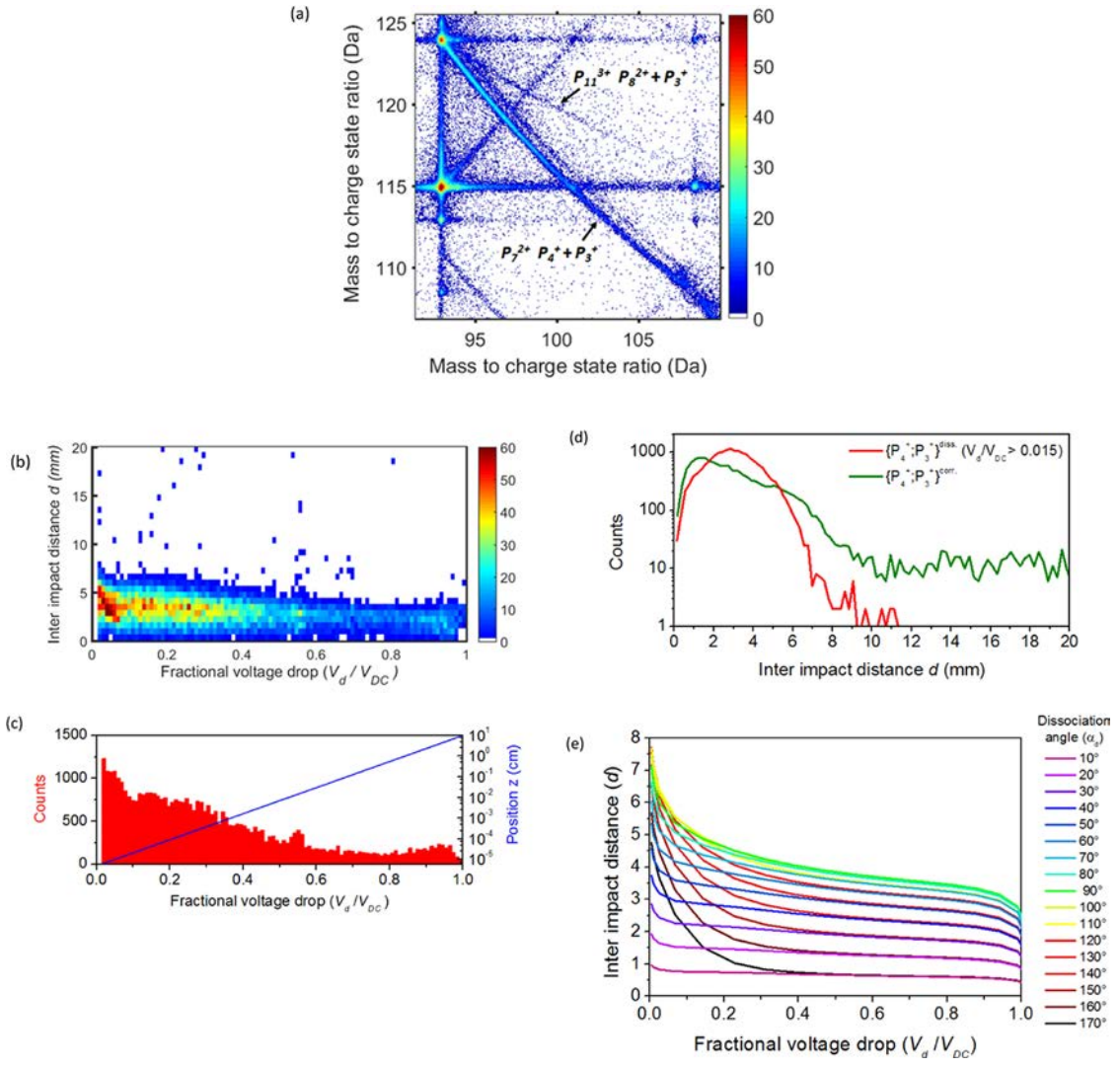

Figure 7. (a) Details of the correlation histogram reported in Figure 5. The dissociation processes $P_7^{2+} \rightarrow P_4^+ + P_3^+$ and $P_{13}^{3+} \rightarrow P_8^{2+} + P_3^+$ are highlighted. The color scale represents the number of detected ion pairs. (b) Histogram of the impact distances between daughter ions as a function of voltage drop and (c) distribution of the dissociation events as a function of V_d/V_{DC} for the dissociation $P_7^{2+} \rightarrow P_4^+ + P_3^+$. The distance from the tip surface as a function of V_d/V_{DC} along the tip−detector axes ($r = 0$) is depicted in blue. The tip surface is at $z_0 = 50$ nm; the detector is placed 10 cm away from the tip. (d) Distribution of distances between impacts associated with multiple events involving $\{P_4^+;P_3^+\}^{diss.}$ and $\{P_4^+;P_3^+\}^{corr.}$ ion pairs. (e) Simulation of the impact distances d as a function of V_d/V_{DC} and the dissociation angle α_d for the dissociation process $P_7^{2+} \rightarrow P_4^+ + P_3^+$.

cations is not driven by the intense DC of the electric field, as recently theorized in the case of the dissociation of ZnO^{2+} cations.[27,51] In fact, delayed dissociations can also be ascribed to phosphorus cations emitted in an excited state, thus explaining the decay in the low field region, a long time after the emission of cations from the tip. A similar behavior was recently observed and explained by dynamic dissociation models for the reactions involving AlN^{2+}, GaN^{2+}, and C_2^{2+} cations.[12,15,52,53]

The distribution of the interimpact distance d associated with $\{P_4^+;P_3^+\}^{diss.}$ ion pairs is reported in Figure 7d. Data reveal a distribution close to 2.8 mm, that is, twice the distance (1.4 mm) found for the whole multiple events of the data set (see Figure 4b). Such a large distance between impacts is caused by Coulomb repulsion between dissociation products.[9,12,13] This is corroborated by numerical calculations that simulate the interimpact distances d associated with the process $P_7^{2+} \rightarrow P_4^+ + P_3^+$ varying both the fractional potential drop V_d/V_{DC} and the dissociation angle α_d (see Figure 2), but keeping the kinetic energy release (KER) due to the Coulomb repulsion equal to 7 eV, to fit the experimental data. In this case, the angle α_d defines the orientation of the P_7^{2+} cation axis with respect to the electric field upon dissociation (considering P_7^{2+} formed by P_3^+ and P_4^+ subunits). At $\alpha_d = 0°$, the P_3^+ is toward the detector, while $\alpha_d = 180°$ corresponds to the P_4^+ toward the detector. The results of such calculations are reported in Figure 7e. The impact distance d decreases with the fractional potential drop V_d/V_{DC} and strongly depends on α_d, with a maximum separation between daughter cations (~8 mm) for dissociation processes occurring close to the tip surface with $\alpha_d = 90°$. In this situation, the ion pair is perpendicular to the flight direction, leading to larger impact distances on the detector. This effect can be appreciated also by observing the experimental data represented in Figure 7b even if a univocal relationship between ion pairs and dissociation angles cannot be established here. Numerical calculations suggest that

$\{P_4^+;P_3^+\}$ ion pairs resulting from dissociation processes close to the tip surface (i.e., $(V_d/V_{DC}) < 0.015$) exhibit interimpact distances close to 4 mm. This value is higher compared to that expected for spatially correlated evaporation phenomena (maximum of the distribution close to 1.4 mm). In principle, the final distribution of distances results from the sum of these two contributions. However, $\{P_4^+;P_3^+\}$ ion pairs exhibiting mass-to-charge ratios close to that expected, respectively, 93 and 124 Da, present a second weak maximum at about 6 mm in their interimpact distance distribution, as reported in Figure 7d. However, the first peak is dominant, showing that correlated events are dominant in number.

Surprisingly, in the correlation histogram of Figure 7a, a second dissociation track was recognized starting from the point {124;93 Da}. This is the clear signature of a dissociation reaction leading to the formation of daughter cation pairs with similar mass-to-charge ratios as those generated by the reaction $P_7^{2+} \rightarrow P_4^+ + P_3^+$. However, a fit of this track using eq 10 reveals that the mother cations have a mass-to-charge-state ratio equal to 113.6 Da. Therefore, data suggest the following dissociation process: $P_{11}^{3+} \rightarrow P_8^{2+} + P_3^+$. It should be noted that the presence of P_{11}^{3+} cations cannot be identified in the mass spectrum shown in Figure 3. This is because the small quantity of P_{11}^{3+} cations is completely hidden between 113 and 115 Da, where the peaks associated with the two In^+ isotopes appear. Also, the study of the mass spectrum associated with the double events only (here not reported) provides no clear evidence of the presence of P_{11}^{3+} cations. This is because just a very small amount of P_{11}^{3+} cations is formed and thus dissociates. Not enough P_{11}^{3+} cations have such a long lifetime to form a peak at 113.6 Da in the mass spectrum. Therefore, only the study of the correlation histogram and an accurate identification of all of the dissociation processes enable exhibiting the formation and the subsequent dissociation of P_{11}^{3+} cations.

The dissociation reactions involving heavier phosphorus cations were finally analyzed. P_8^{2+} and P_9^{2+} cations exhibit a single dissociation pathway. The reactions observed are as follows: $P_8^{2+} \rightarrow P_5^+ + P_3^+$ and $P_9^{2+} \rightarrow P_5^+ + P_4^+$. The dissociation of P_k^{2+} cations with $k \geq 10$ is of greater interest. Multiple dissociation paths may be identified in the correlation diagram shown in Figure 8. The following processes were identified using eq 10: (a) $P_{10}^{2+} \rightarrow P_6^+ + P_4^+$; (b) $P_{10}^{2+} \rightarrow P_7^+ + P_3^+$; (c) $P_{11}^{2+} \rightarrow P_8^+ + P_3^+$; (d) $P_{11}^{2+} \rightarrow P_7^+ + P_4^+$; (e) $P_{12}^{2+} \rightarrow P_8^+ + P_4^+$; and (f) $P_{12}^{2+} \rightarrow P_7^+ + P_5^+$. Lastly, for P_{13}^{2+} cations, four different dissociation reactions were observed. These are as follows: (g) $P_{13}^{2+} \rightarrow P_{10}^+ + P_3^+$; (h) $P_{13}^{2+} \rightarrow P_9^+ + P_4^+$; (i) $P_{13}^{2+} \rightarrow P_8^+ + P_5^+$; and (j) $P_{13}^{2+} \rightarrow P_7^+ + P_6^+$. Again, the formation of P_3^+ and P_4^+ daughter ions is dominant, most likely due to the high stability of such cations.

3.5. Homolytic Phosphorus Cation Dissociation Processes. Only heterolytic dissociations lead to the formation of dissociation tracks. Equation 10 clearly shows that for homolytic dissociation ($m_i = m_p$, for $i = 1, 2$), daughter ions have M/n equal to the expected value. For this reason, dissociation events form a peak on the diagonal of the dissociation diagram, in correspondence to $\{m_p;m_p\}$. However, the repulsive Coulomb force acting between the dissociation products creates in the correlation histogram a very specific track with negative slope (equal to −1), centered at the point $\{m_p;m_p\}$. Homolytic dissociations were recently observed studying $Zn_2O_2^{2+}$ cations, which dissociate into two ZnO^+ fragments during the laser-assisted field evaporation of ZnO,

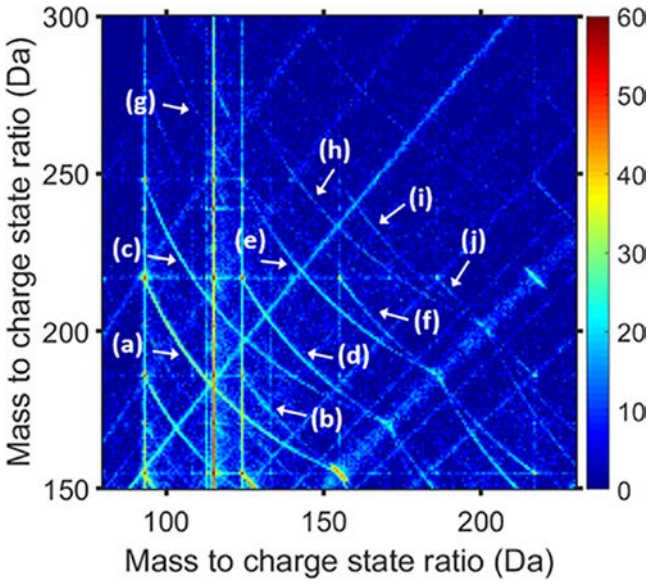

Figure 8. Details of the correlation histograms reported in Figure 5. Some tracks associated with the dissociation reactions (a–j) are indicated by the arrows.

and also in the case of C_2^{2+} cations that dissociate into two C^+ ions.[15,16] The same approach led to the identification of several homolytic dissociations involving phosphorus cations during the evaporation of InP. The reactions identified in the correlation histogram (Figure 5) are as follows: $P_{2k}^{2+} \rightarrow P_k^+ + P_k^+$, with $3 \leq k \leq 7$. Between these reactions, the most intense one is associated with the reaction $P_6^{2+} \rightarrow P_3^+ + P_3^+$. This track is reported in Figure 9.

A more detailed study of the process $P_6^{2+} \rightarrow P_3^+ + P_3^+$ allows revealing information regarding the dissociation dynamic of such a homolytic reaction and the limitation of the detection system that is used here. To do so, all of the ion pairs $\{P_3^+;P_3^+\}$ (i.e., associated with both dissociation and correlated evaporation phenomena) were selected in the correlation

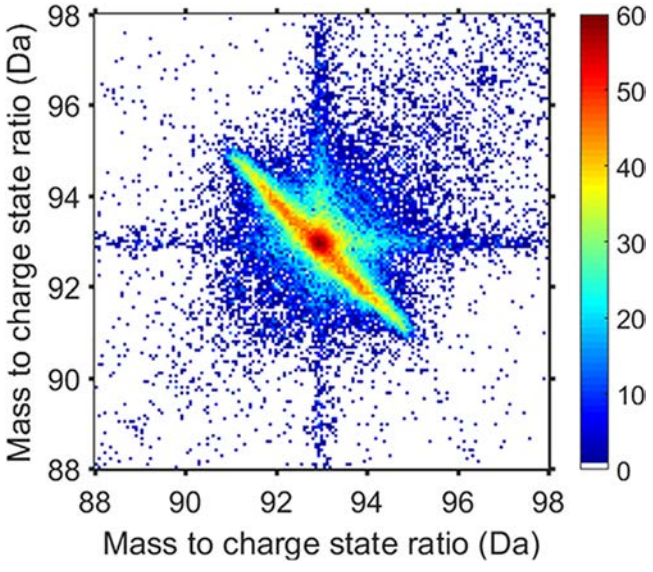

Figure 9. Details of the correlation histograms reported in Figure 5. The very intense negative slope track is associated with the homolytic dissociation reaction $P_6^{2+} \rightarrow P_3^+ + P_3^+$.

histogram represented in Figure 9. Then, the histogram of the mass-to-charge-state ratio difference $m_1 - m_2$ between P_3^+ pairs as a function of their impact distance d was constructed. This histogram is reported in Figure 10a. Experimental data

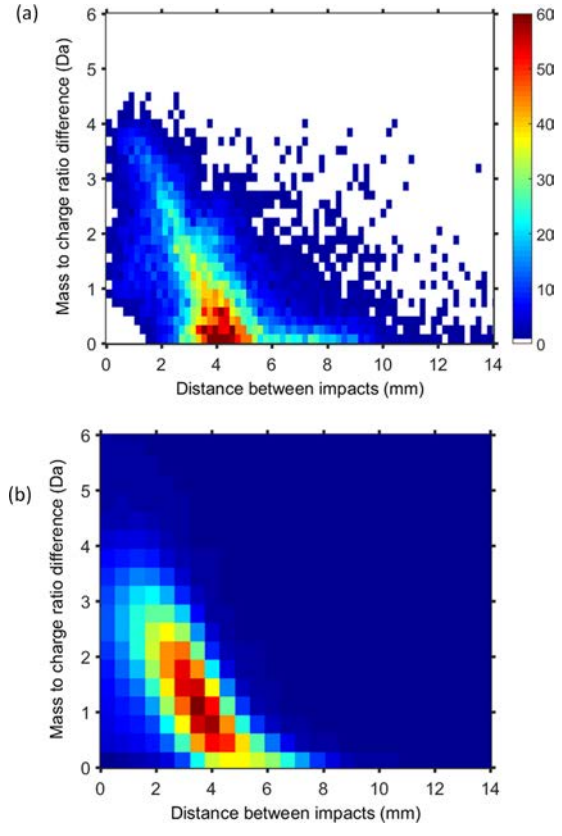

Figure 10. (a) Mass-to-charge-state ratio difference of ion pairs $\{P_3^+, P_3^+\}$ as a function of their impact distance d following the dissociation process $P_6^{2+} \rightarrow P_3^+ + P_3^+$. The color bar represents the number of ion pairs observed. (b) Simulated histogram of the mass-to-charge-state ratio difference between P_3^+ pairs as a function of their impact distance d. The studied dissociation process is $P_6^{2+} \rightarrow P_3^+ + P_3^+$. Simulation parameters: V_{DC} = 11 kV; tip curvature radius R = 100 nm.

reveal the presence of two distributions. The first one is associated with $\{P_3^+;P_3^+\}$ pairs exhibiting a very small mass-to-charge-state ratio difference ($m_1 - m_2 \approx 0$) and impact distances d ranging between 2 and 10 mm, with a maximum close to 4 mm. These pairs are in parts associated with the correlated evaporation of P_3^+ cations, which leave the tip surface during the same laser pulse. The second distribution is due to the detection of $\{P_3^+;P_3^+\}$ pairs following the homolytic dissociations of P_6^{2+} cations. An increase in the mass-to-charge ratio difference ($m_1 - m_2$) up to 4 Da is here associated with a reduction of the pair impact distance d from 5 to 0 mm. It should be interesting to observe that in the circle-shaped region centered at the histogram's origin ($m_1 - m_2 < 0.8$ Da; $d < 1.4$ mm) no ion pair events are observed. This region corresponds to the detector "dead-region". Ion pairs arriving spatially and temporally closer are most likely convoluted in a single signal due to pile-up effects, as previously discussed.

Finally, the parent ion lifetime and the KER due to the Coulomb repulsion were calculated. To do so, the experimental data reported in Figure 10a were compared to simulations considering both ion−ion and ion−tip electrostatic interactions, using the field distribution reported by eqs 3 and 4. The trajectory of the parent ion is simulated until the dissociation time t_d is reached, and it is then replaced in the simulation by the two daughter ions separated by an initial distance d_0 and at an angle α_d (see Figure 2 with respect to the tip axis). Then, the trajectories of the two daughter ions are calculated taking into consideration ion−ion and ion−tip interactions. The initial distance d_0 between the two daughter ions has no physical reality by serving as a way to tune the initial electrostatic potential energy between the two ions before they repel each other. This energy is equal to the KER. This calculation was performed a large number of times with a uniform distribution of angle α_d ranging from 0 to 90°, whereas the values of t_d and d_0 were picked randomly in normal distributions. The mean values and standard deviations of these distributions were varied so as to fit the two-dimensional distribution observed experimentally in Figure 10a (excluding the contribution of the preferential evaporation). The best fit between experimental data and calculations was obtained for a parent molecule lifetime of $t_d = 8.8^{+0.4}_{-7.2}$ ps and a KER = (4.8 ± 1.8) eV. The error bars correspond to the standard deviations that yielded the best fit of the experimental data. Finally, the histogram of the mass-to-charge-state ratio difference between daughter pairs as a function of their impact distance d was calculated. Such a histogram is reported in Figure 10b.

4. CONCLUSIONS

Crystalline InP was analyzed using laser-assisted atom probe tomography. The formation and subsequent dissociation of phosphorous cations during their flight toward the detector are here observed and discussed for the first time. Atom probe tomography allows one both to identify all of the possible dissociation channels for each single cation and to measure important parameters related to dissociation processes such as lifetime, dissociation angles, and kinetic energy released. The analyses of both mass spectrum and dissociation products reveal that P_3^+ and P_4^+ cations are dominant, most likely due to their high stability. A thorough analysis of the data shows also that delayed dissociations occur in correspondence to low field regions, far from the field emitter surface. A direct measure of the molecule lifetime was performed in the case of the dissociation reaction $P_6^{2+} \rightarrow P_3^+ + P_3^+$. A study of the Coulomb repulsion effects observed suggests a lifetime of 8.8 ps. The delayed dissociations revealed during atom probe tomography indicate that phosphorus cations are most likely emitted in an excited state, as recently shown with dynamic dissociation models for the dissociation of cations like AlN^{2+} and GaN^{2+}. In conclusion, this work not only investigates the stability of medium-sized phosphorous cations but also provides operational guidelines to adopt atom probe tomography to study the dynamic of dissociation processes.

AUTHOR INFORMATION

Corresponding Author

E. Di Russo − *UNIROUEN, INSA Rouen, CNRS, Groupe de Physique des Matériaux, Normandie Université, 76000 Rouen, France;* orcid.org/0000-0003-3829-6567; Email: enrico.di-russo@univ-rouen.fr

Authors

I. Blum − *UNIROUEN, INSA Rouen, CNRS, Groupe de Physique des Matériaux, Normandie Université, 76000 Rouen, France;* orcid.org/0000-0002-4729-6510

I. Rivalta − *Dipartimento di Chimica Industriale "Toso Montanari", ALMA MATER STUDIORUM, Università di Bologna, 40126 Bologna, Italia; Univ Lyon, Ens de Lyon, CNRS UMR 5182, Université Claude Bernard Lyon 1, Laboratoire de Chimie, F69342 Lyon, France;* orcid.org/0000-0002-1208-602X

J. Houard − *UNIROUEN, INSA Rouen, CNRS, Groupe de Physique des Matériaux, Normandie Université, 76000 Rouen, France*

G. Da Costa − *UNIROUEN, INSA Rouen, CNRS, Groupe de Physique des Matériaux, Normandie Université, 76000 Rouen, France*

F. Vurpillot − *UNIROUEN, INSA Rouen, CNRS, Groupe de Physique des Matériaux, Normandie Université, 76000 Rouen, France*

D. Blavette − *UNIROUEN, INSA Rouen, CNRS, Groupe de Physique des Matériaux, Normandie Université, 76000 Rouen, France*

L. Rigutti − *UNIROUEN, INSA Rouen, CNRS, Groupe de Physique des Matériaux, Normandie Université, 76000 Rouen, France;* orcid.org/0000-0001-9141-7706

Notes

The authors declare no competing financial interest.

ACKNOWLEDGMENTS

This work was funded by the French National Research Agency (ANR) in the framework of the projects EMC3 Labex AQURATE and ANR-13-JS10-0001-01 TAPOTER and by the Region Normandy in the framework of the RIN IFROST project.

REFERENCES

(1) Rigutti, L.; Mancini, L.; Lefebvre, W.; Houard, J.; Hernàndez-Maldonado, D.; Di Russo, E.; Giraud, E.; Butté, R.; Carlin, J.-F.; Grandjean, N.; et al. Statistical Nanoscale Study of Localised Radiative Transitions in GaN/AlGaN Quantum Wells and AlGaN Epitaxial Layers. *Semicond. Sci. Technol.* **2016**, *31*, No. 095009.

(2) Di Russo, E.; Mancini, L.; Moyon, F.; Moldovan, S.; Houard, J.; Julien, F. H.; Tchernycheva, M.; Chauveau, J. M.; Hugues, M.; Da Costa, G.; et al. Three-Dimensional Atomic-Scale Investigation of ZnO-$Mg_xZn_{1-x}O$ m-Plane Heterostructures. *Appl. Phys. Lett.* **2017**, *111*, No. 032108.

(3) Francaviglia, L.; Tütüncüoglu, G.; Martí-Sánchez, S.; Di Russo, E.; Steinvall, S. E.; Ruiz, J. S.; Potts, H.; Friedl, M.; Rigutti, L.; Arbiol, J.; et al. Segregation Scheme of Indium in AlGaInAs Nanowire Shells. *Phys. Rev. Mater.* **2019**, *3*, No. 023001.

(4) Mancini, L.; Hernández-Maldonado, D.; Lefebvre, W.; Houard, J.; Blum, I.; Vurpillot, F.; Eymery, J.; Durand, C.; Tchernycheva, M.; Rigutti, L. Multi-Microscopy Study of the Influence of Stacking Faults and Three-Dimensional In Distribution on the Optical Properties of m-Plane InGaN Quantum Wells Grown on Microwire Sidewalls. *Appl. Phys. Lett.* **2016**, *108*, No. 042102.

(5) Rigutti, L.; Bonef, B.; Speck, J.; Tang, F.; Oliver, R. A. Atom Probe Tomography of Nitride Semiconductors. *Scr. Mater.* **2018**, *148*, 75−81.

(6) Choi, P. P.; Cojocaru-Mirédin, O.; Wuerz, R.; Raabe, D. Comparative Atom Probe Study of Cu(In,Ga)Se2 Thin-Film Solar Cells Deposited on Soda-Lime Glass and Mild Steel Substrates. *J. Appl. Phys.* **2011**, *110*, No. 124513.

(7) Morris, R. J.; Cuduvally, R.; Melkonyan, D.; Zhao, M.; van der Heide, P.; Vandervorst, W. Atom probe of GaN/AlGaN Heterostructures: The Role of Electric Field, Sample Crystallography and Laser Excitation on Quantification. *Ultramicroscopy* **2019**, *206*, No. 112813.

(8) Di Russo, E.; Blum, I.; Houard, J.; Da Costa, G.; Blavette, D.; Rigutti, L. Field-Dependent Measurement of GaAs Composition by Atom Probe Tomography. *Microsc. Microanal.* **2017**, *23*, 1.

(9) Müller, M.; Saxey, D. W.; Smith, G. D. W.; Gault, B. Some Aspects of the Field Evaporation Behaviour of GaSb. *Ultramicroscopy* **2011**, *111*, 487.

(10) Di Russo, E. Study of the Physical Mechanisms Leading to Compositional Biases in Atom Probe Tomography of Semiconductors. Ph.D. Dissertation, Université de Rouen-Normandie, 2018.

(11) Saxey, D. W. Correlated Ion Analysis and the Interpretation of Atom Probe Mass Spectra. *Ultramicroscopy* **2011**, *111*, 473−479.

(12) Di Russo, E.; Blum, I.; Houard, J.; Gilbert, M.; Da Costa, G.; Blavette, D.; Rigutti, L. Compositional Accuracy of Atom Probe Tomography Measurements in GaN: Impact of Experimental Parameters and Multiple Evaporation Events. *Ultramicroscopy* **2018**, *187*, 126−134.

(13) Santhanagopalan, D.; Schreiber, D. K.; Perea, D. E.; Martens, R. L.; Janssen, Y.; Khalifah, P.; Meng, Y. S. Effects of Laser Energy and Wavelength on the Analysis of $LiFePO_4$ Using Laser Assisted Atom Probe Tomography. *Ultramicroscopy* **2015**, *148*, 57−66.

(14) Estivill, R.; Grenier, A.; Duguay, S.; Vurpillot, F.; Terlier, T.; Barnes, J. P.; Hartmann, J. M.; Blavette, D. Quantitative Analysis of Si/SiGeC Superlattices Using Atom Probe Tomography. *Ultramicroscopy* **2015**, *159*, 223−231.

(15) Peng, Z.; Vurpillot, F.; Choi, P.-P.; Raabe, D.; Gault, B. On the Detection of Multiple Events in Atom Probe Tomography. *Ultramicroscopy* **2018**, *189*, 54−60.

(16) Blum, I.; Rigutti, L.; Vurpillot, F.; Vella, A.; Gaillard, A.; Deconihout, B. Dissociation Dynamics of Molecular Ions in High DC Electric Field. *J. Phys. Chem. A* **2016**, *120*, 3654−3662.

(17) Zanuttini, D.; Blum, I.; Di Russo, E.; Rigutti, L.; Vurpillot, F.; Douady, J.; Jacquet, E.; Anglade, P.-M.; Gervais, B. Dissociation of GaN^{2+} and AlN^{2+} in APT: Analysis of Experimental Measurements. *J. Chem. Phys.* **2018**, *149*, No. 134311.

(18) Huang, R.-B.; Liu, Z.-Y.; Liu, H.-F.; Chen, L.-H.; Zhang, Q.; Wang, C.-R.; Zheng, L. S.; Liu, F.-L.; Yu, S.-Q.; Ma, X.-X. Collision-Induced Dissociation of Mass-Selected Phosphorus Cluster Cations. *Int. J. Mass Spectrom. Ion Processes* **1995**, *151*, 55−62.

(19) Kong, X.-L. Size Effect on the Signal Intensity Difference Between Odd- and Even-Numbered Phosphorus Cluster Ions. *Acta Phys. Chim. Sin.* **2013**, *29*, 486−490.

(20) Padalkar, S.; Riley, J. R.; Li, Q.; Wang, G. T.; Lauhon, L. J. Lift-out Procedures for Atom Probe Tomography Targeting Nanoscale Features in Core-Shell Nanowire Heterostructures. *Phys. Status Solidi C* **2014**, *11*, 656−661.

(21) Blum, I.; Cuvilly, F.; Lefebvre-Ulrikson, W. *Atom Probe Tomography: Put Theory into Practice*; Lefebvre-Ulrikson, W.; Vurpillot, F.; Sauvage, X., Eds.; Academic Press, 2016.

(22) Da Costa, G.; Vurpillot, F.; Bostel, A.; Deconihout, B. Design of a Delay-Line Position-Sensitive Detector with Improved Performance. *Rev. Sci. Instrum.* **2005**, *76*, No. 013304.

(23) Da Costa, G.; Wang, H.; Duguay, S.; Bostel, A.; Blavette, D.; Daconihout, B. Advance in Multi-Hit Detection and Quantization in Atom Probe Tomography. *Rev. Sci. Instrum.* **2012**, *83*, No. 123709.

(24) Vella, A. On the Interaction of an Ultra-Ffast Laser with a Nanometric Tip by Laser Assisted Atom Probe Tomography: A Review. *Ultramicroscopy* **2013**, *132*, 5−18.

(25) Di Russo, E.; Houard, J.; Langolff, V.; Moldovan, S.; Rigutti, L.; Deconihout, B.; Blavette, D.; Bogdanowicz, J.; Vella, A. Optical Shaping of a Nano-Scale Tip by Femtosecond Laser Assisted Field Evaporation. *Appl. Phys. Lett.* **2018**, *112*, No. 143103.

(26) Smith, R.; Walls, J. M. Ion Trajectories in the Field-Ion Microscope. *J. Phys. D: Appl. Phys.* **1978**, *11*, 409−419.

(27) Zanuttini, D.; Blum, I.; Rigutti, L.; Vurpillot, F.; Douady, J.; Jacquet, E.; Anglade, P.-M.; Gervais, B. Electronic Structure and

Stability of the SiO^{2+} Dications Produced in Tomographic Atom Probe Experiments. *J. Chem. Phys.* **2017**, *147*, No. 164301.
(28) Frasinski, L. J.; Codling, K.; Hatherly, P. A. Covariance Mapping: a Correlation Method Applied to Multiphoton Multiple Ionization. *Science* **1989**, *246*, 1029−1031.
(29) Kingham, D. R. The Post-Ionization of Field Evaporated Ions: A Theoretical Explanation of -multiple Charge States. *Surf. Sci.* **1982**, *116*, 273−301.
(30) Mancini, L.; Amirifar, N.; Shinde, D.; Blum, I.; Gilbert, M.; Vella, A.; Vurpillot, F.; Lefebvre, W.; Larde, R.; Talbot, E.; et al. Composition of Wide Bandgap Semiconductor Materials and Nanostructures Measured by Atom Probe Tomography and Its Dependence on the Surface Electric Field. *J. Phys. Chem. C* **2014**, *118*, 24136−24151.
(31) Di Russo, E.; Moyon, F.; Gogneau, N.; Largeau, L.; Giraud, E.; Carlin, J.-F.; Grandjean, N.; Chauveau, J.-M.; Hugues, M.; Blum, I.; Lefebvre, W.; Vurpillot, F.; Blavette, D.; Rigutti, L. Composition Metrology of Ternary Semiconductor Alloys Analyzed by Atom Probe Tomography. *J. Phys. Chem. C* **2018**, *122*, 16704−16714.
(32) Biegelsen, D. K.; Bringans, R. D.; Northrup, J. E.; Swart, L.-E. Surface Reconstructions of GaAs (100) Observed by Scanning Tunneling Microscopy. *Phys. Rev. B* **1990**, *41*, 5701−5706.
(33) Gorman, B. P.; Norman, A. C.; Lawrence, D.; Prosa, T.; Guthrey, H.; Al-Jassim, M. In *Atomic Scale Characterization of Compound Semiconductors Using Atom Probe Tomography*, 37th IEEEE Photovoltaic Specialists Conference, 2011; pp 003357−003359.
(34) Neave, J. H.; Dobson, P. J.; Joyce, B. A.; Zhang, J. Reflection High-Energy Electron Diffraction Oscillations from Vicinal Surfaces—a New Approach to Surface Diffusion Measurements. *Appl. Phys. Lett.* **1985**, *47*, 100−102.
(35) Kelly, T. F.; Larson, D. J. The Second Revolution in Atom Probe Tomography. *MRS Bull.* **2012**, *37*, 150−158.
(36) Liu, Z.-Y.; Huang, R.-B.; Zheng, L.-S. Bare phosphorus and binary phosphide cluster ions generated by laser ablation. *Z. Phys. D* **1996**, *38*, 171−177.
(37) Bacchi, C.; Da Costa, G.; Vurpillot, F. Spatial and Compositional Biases Introduced by Position Sensitive Detection Systems in APT: a Simulation Approach. *Microsc. Microanal.* **2019**, *25*, 418−424.
(38) De Geuser, F.; Gault, B.; Bostel, A.; Vurpillot, F. Correlated Field Evaporation as Seen by Atom Probe Tomography. *Surf. Sci.* **2007**, *601*, 536−543.
(39) Müller, M.; Saxey, D. W.; Smith, G. D. W.; Gault, B. Some Aspects of the Field Evaporation Behavior of GaSb. *Ultramicroscopy* **2011**, *111*, 487−492.
(40) Vella, A. On the Interaction of an Ultra-Fast Laser with a Nanometric tip by Laser Assisted Atom Probe Tomography: A Review. *Ultramicroscopy* **2013**, *132*, 5−18.
(41) Pedrazzini, S.; London, A. J.; Gault, B.; Saxey, D.; Speller, S.; Grovenor, C. R. M.; Danaie, M.; Moody, M. P.; Edmonson, P. D.; Bagot, P. A. J. Nanoscale Stoichiometric Analysis of a High-Temperature Superconductor by Atom Probe Tomography. *Microsc. Microanal.* **2017**, *23*, 414−424.
(42) Bémont, E.; Bostel, A.; Bouet, M.; Da Costa, G.; Chambreland, S.; Deconihout, B.; Hono, K. Effects of Incidence Angles of Ions on the Mass Resolution of an Energy Compensated 3D Atom Probe. *Ultramicroscopy* **2003**, *95*, 231−238.
(43) Arnoldi, L.; Silaeva, E. P.; Vurpillot, F.; Deconihout, B.; Cadel, E.; Blum, I.; Vella, A. Role of the Resistivity of Insulating Field Emitters on the Energy of Field-Ionized and Field-Evaporated Atoms. *Ultramicroscopy* **2015**, *159*, 139−146.
(44) Sévelin-Radiguet, N.; Arnoldi, L.; Vurpillot, F.; Normand, A.; Deconihout, B.; Vella, A. Ion Energy Spread in Laser-Assisted Atom Probe Tomography. *Europhys. Lett.* **2015**, *109*, 37009.
(45) Chen, M. D.; Huang, R. B.; Zheng, L. S.; Zhang, Q. E.; Au, C. T. A Theoretical Study for the Isomers of Neutral, Cationic and Anionic Phosphorus Clusters P5, P7, P9. *Chem. Phys. Lett.* **2000**, *325*, 22−28.
(46) Chen, M. D.; Huang, R. B.; Zheng, L. S.; Au, C. T. The Prediction of Isomers for the Phosphorus Clusters P_7^+. *Main Group Met. Chem.* **1999**, *22*, 479−484.
(47) Mu, L.; Yang, S.; Bao, X.; Yin, H.; Kong, X. Medium-Sized Phosphorus Cluster Cations P_{2m+1}^+ ($6 \leq m \leq 32$) Studied by Collision-Induced Dissociation Mass Spectrometry. *J. Mass Spectrom.* **2015**, *50*, 1352−1359.
(48) Jones, R. O.; Holi, D. Structure of Phosphorus Clusters Using Simulated Annealing—P_2 to P_8. *J. Chem. Phys.* **1990**, *92*, 6710−6721.
(49) Chen, M. D.; Chen, Q. B.; Liu, J.; Zheng, L. S.; Zhang, Q. E.; Au, C. T. Parity Alternation of Ground-State P_n^- and P_n^+ (n = 3−15) Phosphorus Clusters. *J. Phys. Chem. A* **2007**, *111*, 216−222.
(50) Bulgakov, A. V.; Bobrenok, O. F.; Kosyakov, V. I.; Ozerov, I.; Marine, W.; Hedén, M.; Rohmund, F.; Campbell, E. E. B. Phosphorus Clusters: Synthesis in the Gas-Phase and Possible Cagelike and Chain Structures. *Phys. Solid State* **2002**, *44*, 617−622.
(51) Zanuttini, D.; Blum, I.; Rigutti, L.; Vurpillot, F.; Douady, J.; Jacquet, E.; Anglade, P.-M.; Gervais, B. Simulation of Field-Induced Molecular Dissociation in Atom Probe Tomography: Identification of a Neutral Emission Channel. *Phys. Rev. A* **2017**, *95*, No. 061401.
(52) Zanuttini, D.; Blum, I.; Di Russo, E.; Rigutti, L.; Vurpillot, F.; Douady, J.; Jacquet, E.; Anglade, P.-M.; Gervais, B. Dissociation of GaN^{2+} and AlN^{2+} in APT: Analysis of Experimental Measurements. *J. Chem. Phys.* **2018**, *149*, No. 134311.
(53) Zanuttini, D.; Vurpillot, F.; Douady, J.; Jacquet, E.; Anglade, P.-M.; Gervais, B. Dissociation of GaN^{2+} and AlN^{2+} in APT: Electronic Structure and Stability in Strong DC Field. *J. Chem. Phys.* **2018**, *149*, No. 134310.